Surface confinement assisted synthesis of nitrogen-rich hollow carbon cages with Co nanoparticles as breathable electrodes for Zn-air batteries

Jinghao Wu[a,1], Lijun Hu[a,1], Nan Wang[b,1], Yanmin Li[a], Dengke Zhao[b], Ligui Li[b,*], Xinwen Peng[c], Zhiming Cui[d], Li-Jun Ma[e], Yong Tian[a,*], Xiufang Wang[a,*]

[a] *School of Pharmacy, Guangdong Pharmaceutical University, Guangzhou 510006, China*

[b] *Guangzhou Key Laboratory for Surface Chemistry of Energy Materials, New Energy Research Institute, College of Environment and Energy, South China University of Technology, Guangzhou 510006, China*

[c] *State Key Laboratory of Pulp and Paper Engineering, South China University of Technology, 381 Wushan Road, Tianhe District, Guangzhou 510641, China*

[d] *The Key Laboratory of Fuel Cell Technology of Guangdong Province, School of Chemistry and Chemical Engineering, South China University of Technology, Guangzhou 510641, China*

[e] *Key Laboratory of Theoretical Chemistry of Environment Ministry of Education, School of Chemistry and Environment, South China Normal University, Shipai, Guangzhou 510631, China*

ARTICLE INFO

ABSTRACT

Integrating high electrocatalytic activities for both oxygen reduction reaction (ORR) and oxygen evolution reaction (OER) into one nonprecious catalyst entity is highly desired for simplifying the fabrication, operation as well as lowering the production cost of rechargeable Zn-air batteries. Herein, zeolite imidazole framework-67 (ZIF-67) polyhedron nanocrystals are used as N-containing carbonaceous precursors to synthesize N-rich hollow carbon cage composites with Co nanoparticles (Co@NHCC) in the presence of silica nanoparticles and graphitic carbon nitride (g-C_3N_4), an additional high-temperature decomposable nitrogen source. The assembly of dense silica nanoparticles on ZIF-67 surface may serve as hard encapsulation layers, which not only facilitates the incorporation of nitrogen atoms onto graphitized carbon skeletons, but also prevents the ZIF-67 polyhedrons from collapsing and effectively impedes the growth of carbon nanotubes during pyrolysis through surface confinement. Gasification in such an encapsulated environment concurrently generates abundant mesopores in the thin walls of carbonized ZIF-67 polyhedrons, which contributes to a high specific surface area of 910.71 $m^2 g^{-1}$ in the resulting Co@NHCC-800 sample, and hence endows an efficient bifunctional electrocatalyst, with a half-wave potential of +0.837 V for ORR in 0.1 M KOH aqueous solution and a required potential of only +1.512 V to reach 10 mA cm^{-2} in OER catalysis. When used as a breathable electrode for Zn-air batteries, Co@NHCC-800 shows a much higher open-circuit voltage of 1.490 V, a higher discharge power density of 248 mW cm^{-2} as well as a smaller increasement of only 0.100 V for the charge-discharge voltage gap after cycling for 12 h, as compared with commercial Pt/C catalyst. The results in present work pave a new avenue to the synthesis of sophisticated carbon nanomaterials for electrocatalysis.

1. Introduction

Rechargeable Zn-air batteries have attracted considerable attentions due to various advantages, such as the abundant Zn element in earth crust, low production cost, high theoretical energy density, low environment impacts and so on. Moreover, because Zn-air batteries normally employ aqueous electrolytes which have a relatively high boiling point, the potential safety risks encountered in the mainstream lithium-ion batteries that usually utilize volatile and flammable organic liquid electrolytes can be significantly reduced [1–3]. Currently, rechargeable Zn-air batteries represent one of the viable and promising electrochemical energy storage and conversion technologies and hence are growing in popularity for portable electronics, electric vehicles, aerospace applications, storage of intermittent green energy from sunlight and wind etc [4].

For a rechargeable Zn-air battery, its operation entails ORR during discharging and OER that is the reversed process of ORR at the same working electrode during charging. Because these two key reactions

involve multiple complicated reaction pathways and rather sluggish charge-transfer kinetics, highly effective electrocatalysts are generally required to ensure a sufficient output power density for practical applications. To date, the commercially available efficient electrocatalysts for these two reactions are the precious metal-based nanomaterials [5–8]. However, it remains a challenge to find a single precious metal-based bifunctional electrocatalyst that concurrently shows high catalytic activities for both ORR and OER in the same alkaline electrolyte [9,10]. For example, the conventional Pt-based nanomaterials are highly efficient for catalyzing ORR in alkaline electrolyte, but they are inactive for OER catalysis in the same electrolyte [11–13]. In contrast, although nanostructured Ru or Ir oxides are effective for OER electrocatalysis in alkaline electrolyte, their ORR electrocatalytic activities are rather limited in the same solution [14,15]. These situations make the fabrication and operation of rechargeable Zn-air batteries become more complicated and are not beneficial to production cost reduction. Moreover, some intrinsic disadvantages of precious metals, such as scarcity and high cost, have also severely impeded the massive production of precious metal-based electrocatalysts for rechargeable Zn-air batteries and other electrochemical energy storage and conversion devices [16–18]. Therefore, exploration of novel nonprecious metals-based electrocatalysts that integrate efficient ORR and OER catalytic activities in the same working electrolyte is of particular interest from the viewpoints of academic research and practical applications [19–23].

Recently, heteroatom (N, P, S, etc.) doped carbons as well as their composites with nonprecious transition metal (Co, Fe, Mo, etc.) nanomaterials are considered as a class of potential alternatives to the conventional precious-metal electrocatalysts [24,25] not only because of their low cost and remarkable multifunctional catalytic activities, but also due to various other advantages, such as ease of preparation, highly tunable composition/structure/morphology, excellent long-term operation stability, abundant available source materials [26–30] and so on. As for the preparation of these carbon composite electrocatalysts, metal organic-frameworks (MOFs) represent one of the promising precursors due to its high surface area, adjustable porous structure, relatively high content of N, S, P, B or other heteroatoms, variable composition as well as diverse nanostructures [31–34]. Of the MOFs, zeolite imidazole framework (ZIF) is a typical nitrogen-rich carbonaceous scaffold that comprises direct coordination bonding between the transition metal cations and the N-containing sites. These nanostructured ZIFs can be further converted to the carbon nanomaterials with homogeneously distributed M-Nx/C active species for efficient ORR and OER electrocatalysis [35–37]. However, the metal atoms in ZIFs tend to aggregate into large particles with a diameter in the range of tens of nanometer to submicron during common high-temperature carbonized/pyrolysis process [38–40], and usually results in a decreased

electrocatalytic activity. Therefore, it is highly desirable to find novel and facile way to impede the excessive growth of metal-containing active species. Besides the M-Nx/C species, nitrogen single-atom sites on graphitized carbon skeleton, including graphitic N and pyridinic N, are also reported to be active for ORR and OER electrocatalysis [41–43]. Therefore, a relatively high content of nitrogen is a prerequisite for efficient N-doped carbons. Yet, nitrogen in the widely used ZIF ligand imidazole is highly volatile. Therefore, before reaching the desired pyrolysis temperature, most of nitrogen has been released, without incorporating onto the gradually formed graphitized carbon skeletons, hence resulting in carbon catalysts with a low content of nitrogen as well as poor oxygen electrocatalytic activities. Moreover, during the pyrolysis process, the intrinsic porous nanostructured ZIFs usually collapse and finally fuse together to form carbon nanotubes (CNT) with intact surface, which drastically reduce the surface area and generally lead to unsatisfied catalytic activity. These two situations also call for exploration of simple preparation methods to reserve nitrogen and the unique nanostructure of ZIFs precursors during high-temperature pyrolysis process, so that cost-effective, bifunctional electrocatalysts can be viably synthesized for efficient ORR and OER in rechargeable Zn-air batteries [44,45], which is the primary motivation of present work.

In present work, we used ZIF-67 as precursor, and g-C$_3$N$_4$ as the additional high-temperature decomposed nitrogen source to prepare N-doped carbon composite catalysts. After deposition of dense silica nanoparticles on the surface of ZIF-67 polyhedron crystals, polyhedron-like hollow carbon nanocages with porous thin graphitized carbon wall were obtained. Whereas, without the addition of silica sol during sample preparation, the ZIF-67 polyhedron crystals collapsed and fused together to form large irregular particles with a significantly lower nitrogen content, and concurrently fostered the growth of bamboo-like carbon nanotubes (CNTs) encapsulating large Co nanoparticles. The preservation of the polyhedron-like morphology of ZIF-67 crystals contributes to a high surface area and abundant mesoporous structures, which help expose the catalytic active sites and also boost the mass transfer process, leading to efficient oxygen reversible electrocatalysts. When utilized as an air-breathable electrode in a rechargeable Zn-air battery, it showed a much higher open circuit voltage of 1.49 V than the commercial Pt/C catalyst, as well as a maximum discharge power density of 248 mW cm^{-2} at 10 mA cm^{-2} and only a slight increase in the charge-discharge voltage gap after continuously cycling for 12 h. The results in present work highlight the importance of morphology engineering in carbon-based electrocatalysts, and also pave an avenue to the preparation of nanostructured multifunctional electrocatalysts from MOFs.
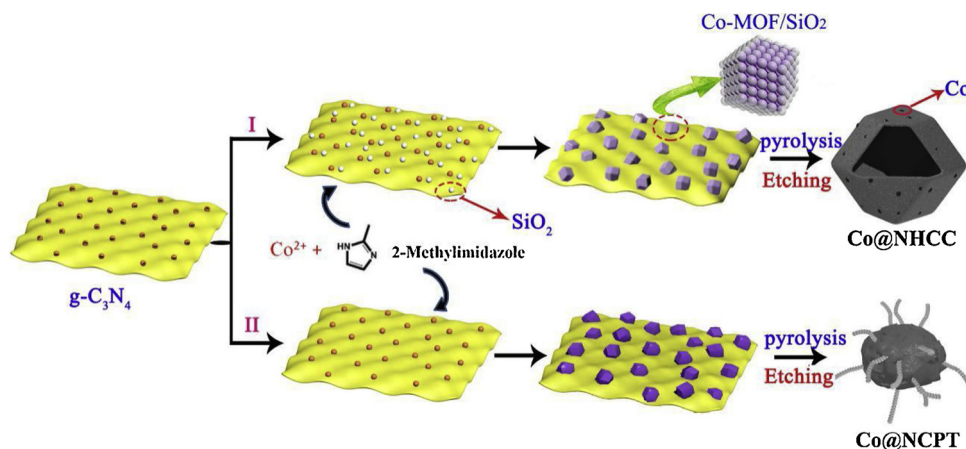
Scheme 1. A series of schematic diagrams for illustrating the synthesis of Co@NHCC and Co@NCPT samples.
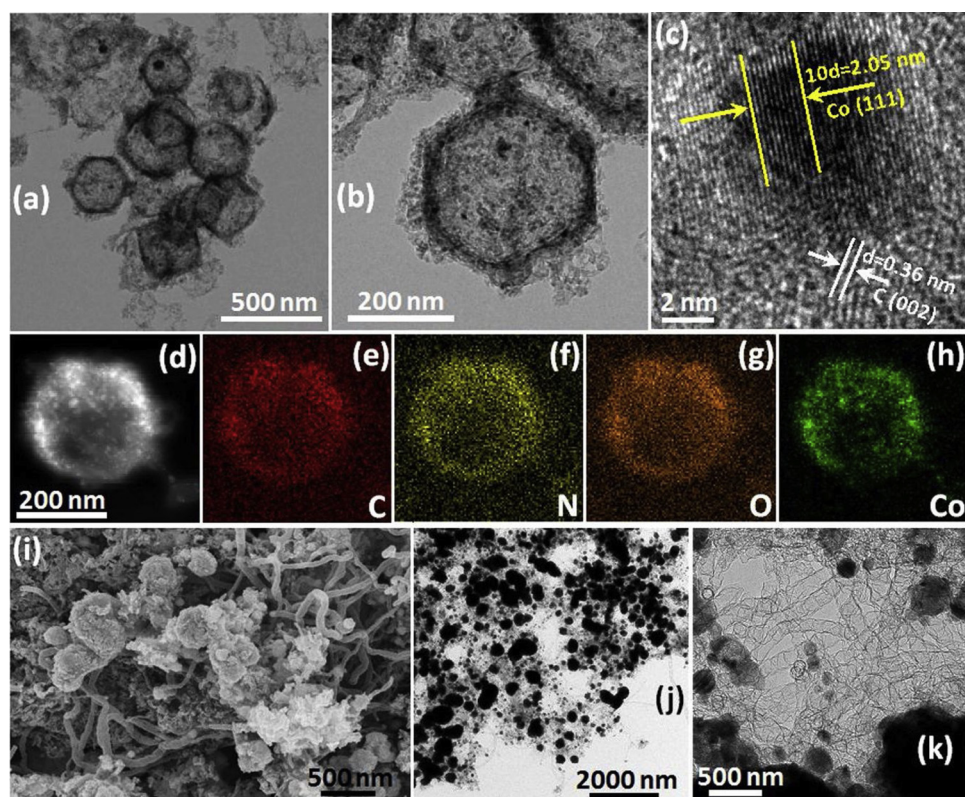
Fig. 1. Typical TEM images of (a, b) Co@NHCC-800 and (c) the corresponding HR-TEM image of Co@NHCC-800. (d) The HAADF-STEM image of Co@NHCC-800 and the corresponding elemental mapping images of (e) C, (f) N, (g) O, and (h) Co. (i) SEM image of Co@NCPT-800 sample. TEM images for showing the dark-contrast nanoparticles embedding in the (j) irregular large particles and (k) CNTs for Co@NCPT-800 sample.

2. Experimental section

2.1. Catalyst synthesis

The typical synthesis procedure is illustrated in Scheme 1. In brief, g-C₃N₄ was prepared by annealing of melamine at 600 °C for 3 h under nitrogen atmosphere. Then, 2 mmol g-C₃N₄ was dispersed in 100.0 mL methanol by sonication. Afterwards, 0.6 mmol Co(NO₃)₂·6H₂O, 5 mmol 2-methylimidazole and 12.0 mL silica sol (6.0 mg mL^{-1}) were simultaneously added into the methanol dispersion and stirred for 4 h, followed by incubation at room temperature for 12 h. The dark blue precipitates were separated by centrifugation, washed with methanol and deionized water for several times, and then dried at 50.0 °C for 12 h in a vacuum oven. The dried powder was further ground with mortar and pestle, affording the composite precursor Co-MOF/SiO₂/C₃N₄.

To obtain the catalysts, the as-prepared precursor was pyrolyzed in Ar atmosphere at different temperature (700, 800, and 900 °C, respectively) for 2 h with a ramping rate of 5 °C min^{-1}. After cooling down to room temperature, thus-obtained black solid products were collected and etched with diluted hydrofluoric acid solution for 24 h at room temperature, followed by centrifugation and rinsing with deionized water for several times and subsequently drying at 50 °C for overnight. The resulting catalysts were referred to as Co@NHCC-T, with T being the pyrolysis temperature.

Control samples synthesized with a similar fashion but without the addition of silica sol were also prepared and referred to as Co@NCPT.

2.2. Characterizations

Powder X-ray diffraction (XRD) spectra were acquired on a Bruker D8 diffractometer with Cu Kα radiation beam. Transmission electron microscopic (TEM) measurements were performed on a Tecnai G2-F20 microscope with an acceleration voltage of 100 kV. The corresponding TEM samples were prepared by drop casting a catalyst dispersion directly onto a copper grid with a holey carbon film as supporting layer.

X-ray photoelectron spectroscopy (XPS) was acquired on a Phi X-tool instrument. Inductively coupled plasma − atomic emission spectrometry (ICP-AES) measurements were carried out with a Liberty-ax instrument. Barrett-Emment-Teller (BET) surface area and the corresponding pore size distribution was determined with N₂ adsorption/adsorption isotherms at 77 K on a Quantachrome Autosorb-iQ2 instrument.

2.3. Electrochemical measurements

Electrochemical measurements were conducted with a CHI 750E electrochemical workstation (CH Instruments Inc.) at room temperature. The catalyst-coated glassy carbon electrode (GCE) was used as the working electrode, while a platinum wire and a commercial Ag/AgCl electrode were employed as the counter electrode and reference electrode, respectively. The potential of Ag/AgCl reference electrode was calibrated with respect to a reversible hydrogen electrode (RHE) by the formula of $E_{RHE} = E_{Ag/AgCl} + 0.966$ V in all measurements.

Identification of the ORR activity was performed in a 0.1 M KOH aqueous solution. To prepare a catalyst modified electrode, the catalyst was dispersed into a homogeneous solution containing commercial nafion (5.0 wt. %), isopropanol and deionized water at a volume ratio of 0.025:1:4 to form a homogeneous suspension with a catalyst concentration of 2.0 mg mL^{-1}, and then a calculated amount of the catalyst suspension was evenly deposited onto the clean GCE surface with a syringe and dried at room temperature. All cyclic voltammograms (CV) were obtained at a scan rate of 10 mV s^{-1}. The linear sweep voltammograms (LSV) were determined in oxygen-saturated 0.1 M KOH solution with an electrode rotation rate ranging from 100 to 2500 rpm. The potential of disk electrode was swept in the range from −0.04 V to + 1.16 V while the potential of ring electrode was set at +0.500 V during measurement.

OER tests were also performed with the same electrochemical setup but in a 1.0 M KOH aqueous solution. The working electrode was a Rotating Ring Disk Electrode (RRDE) (diameter: 5.0 mm). A platinum
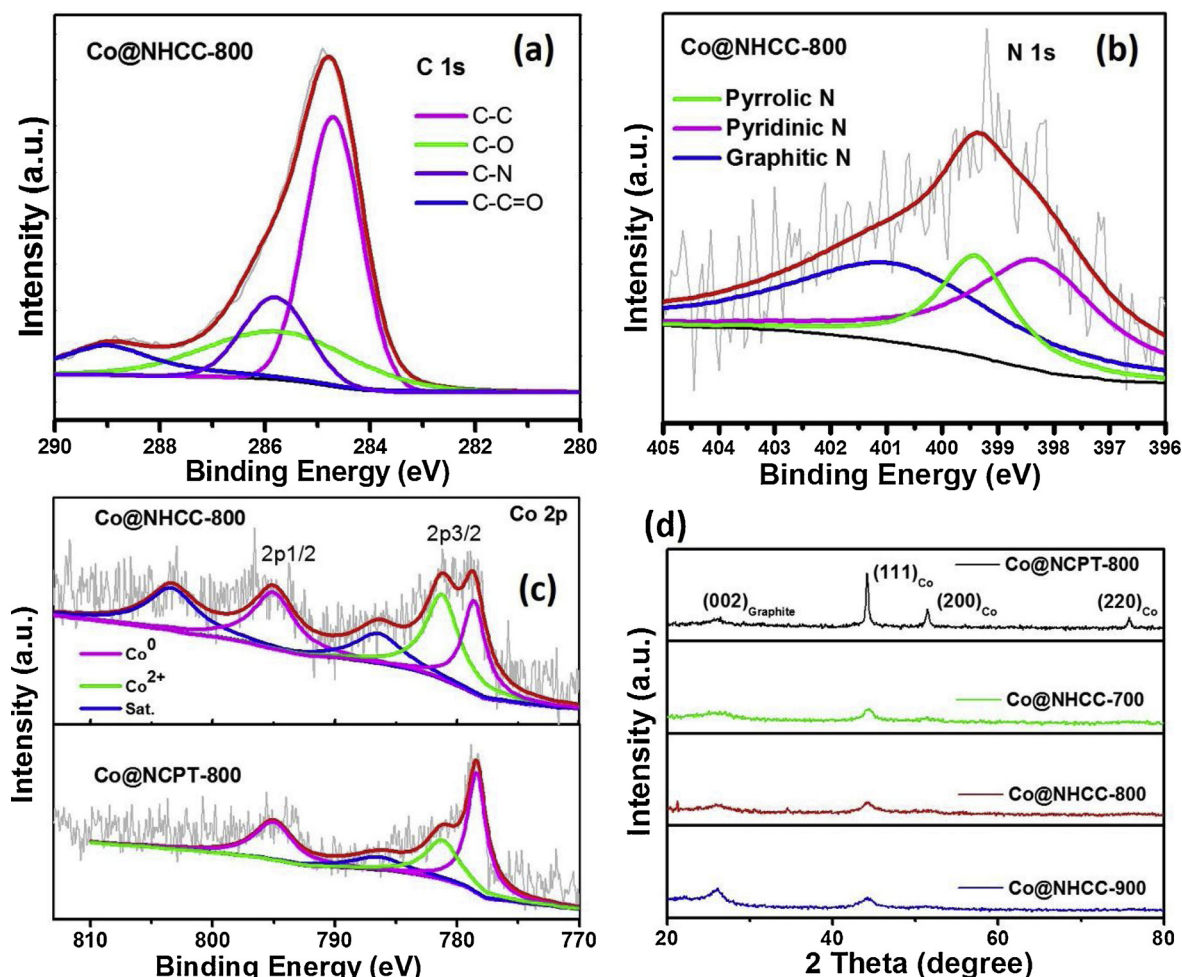
Fig. 2. High-resolution XPS spectra of the (a) C1s, (b) N1s and (c) Co2p electrons for Co@NHCC-800 sample. (d) XRD patterns of different catalyst samples.

wire and a commercial Ag/AgCl electrode ($E_{Ag/AgCl}$ = E_{RHE} + 0.966 V) were utilized as the counter electrode and reference electrode, respectively.

The influence of capacitive effects was eliminated through background correction, i.e. directly subtracting the LSV data measured in N_2-saturated 0.1 M KOH from that determined in O_2-saturated 0.1 M KOH. In the course of ORR test, we carried out iR compensation by using the electrochemical workstation (CH Instruments, Inc., Model CHI 750E). But for OER, the LSV curves were iR compensated after the electrochemical impedance spectra (EIS) measurement, not during the tests.

3. Results and discussion

The morphology of the resulting Co@NHCC samples were observed by TEM measurements. As depicted in Fig. 1a, polyhedron-like hollow cages with a lateral size of 200 to 300 nm are observed, indicating the morphology of ZIF-67 polyhedron nanocrystals (Figure S1a) is largely reserved after pyrolysis treatment. From the TEM image with a higher magnification (Fig. 1b), dark-contrast nanoparticles with a diameter ranging from a few nanometers to about 50.0 nm are observed. The wall thickness of polyhedron-like hollow nanocages is in the range of 25.0 to 35.0 nm. Moreover, one can also find that the thin wall of polyhedron-like nanocages comprises abundant nanoscale porous structures that might help promote the transfer of correlated species for oxygen electrocatalysis. From the corresponding HR-TEM image depicted in Fig. 1c, lattice fringes with a d-spacing of 0.205 nm are well resolved for the dark-contrast nanoparticles, which coincide with the (111) plane of

face-centered cubic phase Co, signifying the formation of crystalline Co nanoparticles. Whereas, wavy lattice fringes with a d-spacing of about 0.364 nm are observed on the low-contract background, which are consistent with the (002) plane of graphitic carbon, indicating the formation of highly graphitized carbons. Fig. 1d–h show the representative high-angle annular dark-field scanning transmission electron microscopy (HAADF-STEM) image and the 2D distribution of C, N, O and Co elements, where one can find that C, N and O elements are evenly distributed on the polyhedron-like Co@NHCC particle, while the distribution of Co element is more localized and resembles to that of the bright particles in Fig. 1d, again indicative of the formation of tiny Co nanoparticles on graphitized polyhedron-like carbon nanocages.

In contrast, the control sample Co@NCPT-800 that was prepared with a similar fashion to Co@NHCC-800 but without the addition of silica sol during synthesis is mainly composed of carbon nanotubes (CNTs) with either one of their terminals connecting to large irregular particles (Fig. 1i). These large irregular particles are attributed to the collapsed and fused MOF carbon cages. A closer look at the large irregular particles reveals that a large number of dark-contrast nanoparticles which are attributed to Co nanoparticles are embedded in the irregular particles (Fig. 1j). Whereas, only sporadic dark-contrast nanoparticles are embedded in the bamboo-like CNTs (Fig. 1k). Taken the above observations into account, one can conclude that the presence of a large number of silica nanoparticles on the surface of ZIF-67 polyhedron nanocrystals (Fig. S1b) may serve as a hard encapsulation layer that can strongly influence on the morphology and composition of the final carbon products. On one hand, with the presence of this hard silica encapsulation layer, the surface of the ZIF-67 polyhedron crystals is

strongly confined to facilitate carbonization, hence the polyhedron structure of parent ZIF-67 is largely preserved and concurrently the growth of CNTs is significantly suppressed during pyrolysis. On the other hand, the inner parts of ZIF-67 polyhedron crystals are less confined by the dense silica nanoparticle layer on their surface, and hence are easier to decompose into volatile species, leading to the formation of hollow carbon cages. While directly pyrolyzing the ZIF-67 polyhedron crystals without the presence of dense silica nanocrystals-based hard encapsulation layer inevitably causes the collapse and fusion of ZIF-67 polyhedron crystals [44], and concurrently the growth of CNT appears, as evidenced by the TEM results depicted in Figure S2 and Fig. 1i.

XPS measurements were subsequently conducted to identify the surface composition of the nanocomposites. As shown in Figure S3, elements C, N, O and Co were observed on the Co@NHCC-800 sample and also the control sample Co@NCPT-800. As for the high-resolution XPS spectrum for C1s electrons of Co@NHCC-800 (Fig. 2a), it can be deconvoluted into four different peaks at about 284.7 eV, 285.7 eV, 285.8 eV and 289.1 eV, which are derived from C−C, C−N, C−O and C−C = O species, respectively [46]. The observation of C−C = O and C−O moieties indicates the presence of partial oxidation on the resulting carbon skeletons after pyrolyzing at 800 °C. Similarly, the high resolution XPS spectrum for N1s electrons (Fig. 2b) can be apparently de-convoluted into three different peaks at about 398.3 eV, 399.5 eV and 400.9 eV, which are attributed to the pyridinic N, pyrrolic N and graphitic N species, respectively [47]. As for Co@NHCC-800 sample, it has a total nitrogen content of 7.79 at.% that is the highest among the Co@NHCC-T series, with 7.28 at.% for Co@NHCC-700 and 3.20 at.% for Co@NHCC-900. Moreover, the content of graphitic N and pyridinic N, two potential nitrogen active species for oxygen electrocatalysis [48,49], in Co@NHCC-800 is about 6.34 at.%, which is also much higher than the 4.23 at.% for Co@NHCC-700, and 1.37 at.% for Co@NHCC-900. Fig. 2c depicts the high-resolution XPS spectrum of Co 2p electrons for Co@NHCC-800 (upper section) and Co@NCPT-800 (bottom section), where two core-level signals are observed, with the one at about 779.8 eV corresponding to the $Co2p_{3/2}$ electrons while the one at about 796 eV being derived from $Co2p_{1/2}$ electrons. After deconvolution, three pairs of peaks can be identified for Co@NHCC-800 sample, and the deconvoluted peak centered at 781.2 eV is ascribed to Co^{2+}, with a pair of satellite peaks appearing at 786.4 eV and 803.3 eV, while the other two deconvoluted peaks at 778.4 eV and 779 eV are attributed to metallic Co [50–53]. One may note that the binding energy peaks for Co_{2p} electrons in Co@NCPT-800 basically locate at the same positions as that of Co@NHCC-800, which indicates that the chemical states of element Co in Co@NCPT-800 sample are identical to Co@NHCC-800, i.e. presenting in the form of Co^{2+} and metallic Co°. However, careful analysis reveals that the integrated Co^{2+} peak of Co 2p3/2 electrons in Co@NHCC-800 sample is apparently higher than its Co° peak, while the intensity of Co° peak of Co 2p3/2 electrons in Co@NCPT-800 is about three-times higher than that of Co^{2+} peak. These observations suggest that besides the formation of metallic Co nanoparticles, nearly half of the Co atoms are coordinating with element N to form the catalytic active Co-Nx-C species in the resulting Co@NHCC-800 sample [54,55]; whereas, Co atoms in Co@NCPT-800 sample predominantly present in the form of Co°, with only a small partial of Co-Nx-C species. These observations clearly signify that most of the Co atoms in Co@NCPT-800 aggregates to form large nanoparticles, while Co atoms are largely atomically dispersed to form the Co-Nx-C active species in Co@NHCC-800 sample mostly due to the surface confinement of dense silica nanoparticles layer.

The detailed compositions for all the investigated samples are summarized in Table 1, where one can find that the Co@NHCC-T series samples have a much higher content of N but a lower content of Co than the Co@NCPT-800 sample. This is most probably because that the high density of silica nanoparticles on the surface of ZIF-67 polyhedron crystals may serve as hard encapsulation layer, which not only help

preserve the light-weight element N on the resulting carbon matrix to form a high content of nitrogen dopant, similar to that observed by Ding et al. who used NaCl as the shape-fixing agent for the high-yield synthesis of one-dimensional N-rich carbons [56], but also form large amount of mesopores on the carbonized products. Moreover, this hard encapsulation layer can prevent the polyhedron-like ZIF to collapse [57], and hence contribute to a high surface area for efficiently exposing the active sites and guaranteeing a fast mass transfer to ensure a high catalytic activity. The low content of Co element in Co@NHCC-T series samples is attributed to the reason that excessive Co-containing species in polyhedron-like carbon cage are etched away because the wall of polyhedron-like carbon cage is highly porous, while the Co and Co-containing nanoparticles in Co@NCPT-800 sample are largely reserved because most of them are still encapsulated in the bamboo-like CNTs or the intact particles (Fig.1j–k).

XRD measurements were then performed to study the crystal structure of the composites. As depicted in Fig. 2d, four distinct diffraction peaks are observed at about 2θ of 25.4°, 44.2°, 51.3° and 76.0°, corresponding to the (002) plane of graphitic carbon and the (111), (200) and (220) planes of fcc phase metallic Co. Note that the diffraction peaks are observed to appear at nearly the same positions for all the investigated samples, indicating the presence of identical crystalline phase of Co in these samples. However, one can find that the intensity of Co (111) peak at about 2θ of 44.2° (JSPDS Card# 65–1765) for the series Co@NHCC-T samples is much lower than that of Co@NCPT-800, indicative of the presence of lower content of metallic Co in the series of Co@NHCC-T samples. In addition, no apparent XRD peaks are observed for cobalt oxides, carbides, etc., again indicating the Co^{2+} species observed by XPS measurements in Co@NHCC-T samples may coordinate with nitrogen on the skeleton of carbon to form Co-N$_x$-C species that is reported to be one of the catalytic active species for oxygen electrocatalysis with Co-N/C catalysts [58,59].

The specific surface area and the porous structures of the above investigated samples were further analyzed with BET measurement. Based on the N_2 adsorption/desorption isotherms depicted in Fig. 3a, one can find that all the investigated samples show typical IV isotherms with obvious hysteresis loops, indicative of the presence of mesoporous structures. Among the series, Co@NHCC-800 shows the highest BET surface area of 910.71 $m^2 g^{-1}$. The pore diameter for the four investigated catalysts is mainly within the range of 2.0–4.0 nm (Table 1). Remarkably, the Co@NHCC-800 sample contains much more mesoporous structures than the other two series samples (Fig. 3b), with a content of about 0.50 $cm^3 g^{-1}$ at ca. 2.40 nm and 1.10 $cm^3 g^{-1}$ at about 3.60 nm. As for the control sample Co@NCPT-800, the content of mesopores is much lower than Co@NHCC-800, which signifies the importance of silica hard encapsulation layer in the formation of highly porous structures. The high surface area and abundant mesoporous structures in Co@NHCC-800 can help maximize the exposure of active sites and also increase the mass transfer process [60,61] which should lead to better electrocatalytic performance.

The ORR catalytic activity of the composite catalysts was evaluated in an oxygen-saturated 0.1 M KOH aqueous solution. As for the rotating ring-disk electrode (RRDE) voltammogram (Fig. 4a), the current density markedly increases when the electrode potential is negatively swept across +1.000 V for Pt/C (20 wt.%), +0.938 V for Co@NHCC-800, and +0.905 V for Co@NHCC-700, Co@NHCC-900 and Co@NCPT-800 samples. Hence, the Co@NHCC-800 sample shows the highest onset potential among the three Co@NHCC-T samples and higher than that of Co@NCPT-800 catalyst. Similarly, the diffusion-limiting current density is also significantly affected by the presence of silica hard templates and calcination temperatures. For example, at +0.200 V, Co@NHCC-800 sample shows a diffusion-limiting current density of 5.813 mA cm^{-2}, which is higher than the 3.524 mA cm^{-2} for Co@NHCC-700, 4.785 mA cm^{-2} for Co@NHCC-900 and 3.887 mA cm^{-2} for Co@NCPT-800. The corresponding half-wave potential was determined to be +0.837 V for Co@NHCC-800, which is also much higher than the

Table 1
Summary of the surface area, average pore size and elemental compositions determined by XPS measurements for different samples.

Sample	Surface area (m² g⁻¹)	Average pore (nm)	C (at.%)	O (at.%)	Co (at.%)	Total N (at.%)	Pyridinic N (at.%)	Pyrrolic N (at.%)	Graphitic N (at.%)
Co@NHCC-700	60.27	2.97	76.79	14.76	1.17	7.28	1.63	3.05	2.60
Co@NHCC-800	910.71	3.58	81.65	8.20	2.36	7.79	3.21	1.45	3.13
Co@NHCC-900	353.96	2.66	83.26	11.67	1.87	3.20	0.12	1.83	1.25
Co@NCPT-800	367.94	2.39	76.33	17.46	4.81	1.40	0.49	0.32	0.59
Co@NHCC-800-12 h (Cycled in Zn-air battery)	/	/	78.57	14.24	2.01	5.05	1.74	1.23	2.08

+0.791 V for Co@NHCC-700, +0.809 V for Co@NHCC-900 and the +0.756 V for Co@NCPT-800, but highly comparable to the +0.840 V for commercial Pt/C catalyst. These observations again demonstrate the importance of silica hard encapsulation layer in the synthesis of highly active ORR catalysts and also signify that the Co@NHCC-800 sample is the best one among the series. Note that the small peak appeared at about +0.740 V in the ORR LSV curve of Co@NHCC-800, i.e. before the limiting current plateau, comes from the reduction of dissolved oxygen in the abundant pores of this sample [62]. In contrast, for Co@NHCC-700, Co@NHCC-900, Co@NCPT-800 and Pt/C catalyst, their surface area is not as high as that of Co@NHCC-800 and comprises less pores, hence no such a small peak can be observed.

The correlated number of electron transfer (*n*) and hydrogen peroxide yield can be calculated according to Eq. 1 and Eq. 2, respectively.

$$n = \frac{4I_{Disk}}{I_{Ring}/N + I_{Disk}} \tag{1}$$

$$H_2O_2 \% = \frac{200I_{Ring}/N}{I_{Ring}/N + I_{Disk}} \tag{2}$$

Where N is the collection efficiency of the RRDE, with a calculated value of 37% according to the configuration of RRDE used in present work [63,64]; I_{Disk} and I_{Ring} are the voltammetric current detected on the disk and ring electrode, respectively [65,66]. As shown in Fig. 4b, one can find that the series Co@NHCC-T samples show an apparently higher *n* value and lower hydrogen peroxide yield than the Co@NCPT-800 in a wide potential range from 0 to +0.800 V. For example, at +0.800 V that is in the low overpotential region, the number of electron transfer value *n* is determined to be 3.57 for Co@NHCC-700, 3.84 for Co@NHCC-800, 3.68 for Co@NHCC-900 and 3.52 for Co@NCPT-800. The corresponding hydrogen peroxide yield determined at +0.800 V is 6.4% for Co@NHCC-800, a value that is somewhat higher than that of commercial Pt/C catalyst (2.7%) but significantly lower than the 20.6% for Co@NHCC-700, 14.5% for Co@NHCC-900 and 20.7% for Co@NCPT-800. These results clearly signify the important

role of silica hard encapsulation layer in guiding the ORR along the preferred 4e⁻ pathway. Additionally, one should note that Co@NHCC-800 shows the highest onset potential, half-wave potential and number of electron transfer among the three Co@NHCC-T samples, indicating that the optimized pyrolysis temperature in synthesis is at about 800 °C.

From Figure S4c, one can observe that the diffusion-limiting current steadily increases with stepwise increasing the rotation rate of RRDE from 400 to 2025 rpm. The corresponding Koutecky–Levich (K–L) plots (Figure S5) for all the investigated catalysts show a linear correlation with highly comparable slopes, which indicates that the ORR proceeded on these catalysts follows a first-order reaction kinetics, i.e. the apparent reaction rate is proportional to the dissolved oxygen concentration in the electrolyte.

The Tafel plots for all the investigated catalysts are depicted in Fig. 4c. Normally, the Tafel slope for an ORR is close to 120 or 60 mV dec⁻¹, signifying a pseudo-two-electron reaction [67] or first-electron reduction of oxygen [68] as the rate-limiting step. From Fig. 4c, the Tafel slope is determined to be 74 mV dec⁻¹ for Co@NHCC-700, 67 mV dec⁻¹ for Co@NHCC-800, 78 mV dec⁻¹ for Co@NHCC-900 and 72 mV dec⁻¹ for Co@NCPT-800, very close to that of commercial Pt/C catalyst (56 mV dec⁻¹). Therefore, one can conclude that the mechanism of ORR proceeded on the surface of these catalysts is similar to commercial Pt/C catalyst, that is, the first-electron reduction of oxygen dominates the entire ORR kinetics.

The operation stability of the Co@NHCC-800 ORR catalyst is then evaluated by chronoamperometric method. As depicted in Fig. 4d, after continuously operating for 30,000 s the electrode loaded with Co@NHCC-800 catalyst is able to maintain 92.8% of its initial current, while the reference electrode modified with commercial Pt/C catalyst shows a rapid decrease at the first 5000 s and finally can only retain 80.5% of its initial current value, which suggests that Co@NHCC-800 has a much higher operation stability than the commercial Pt/C (20 wt.%) catalyst.

Interestingly, the aforementioned catalysts also showed apparent OER activity, hence they can serve as bifunctional electrocatalyst for oxygen reversible catalysis, a distinct property that is highly desired for
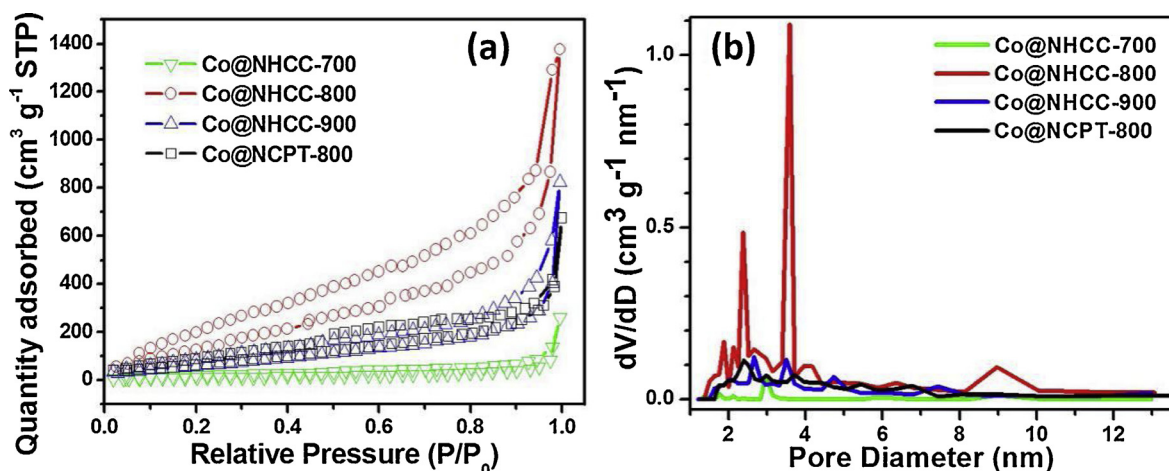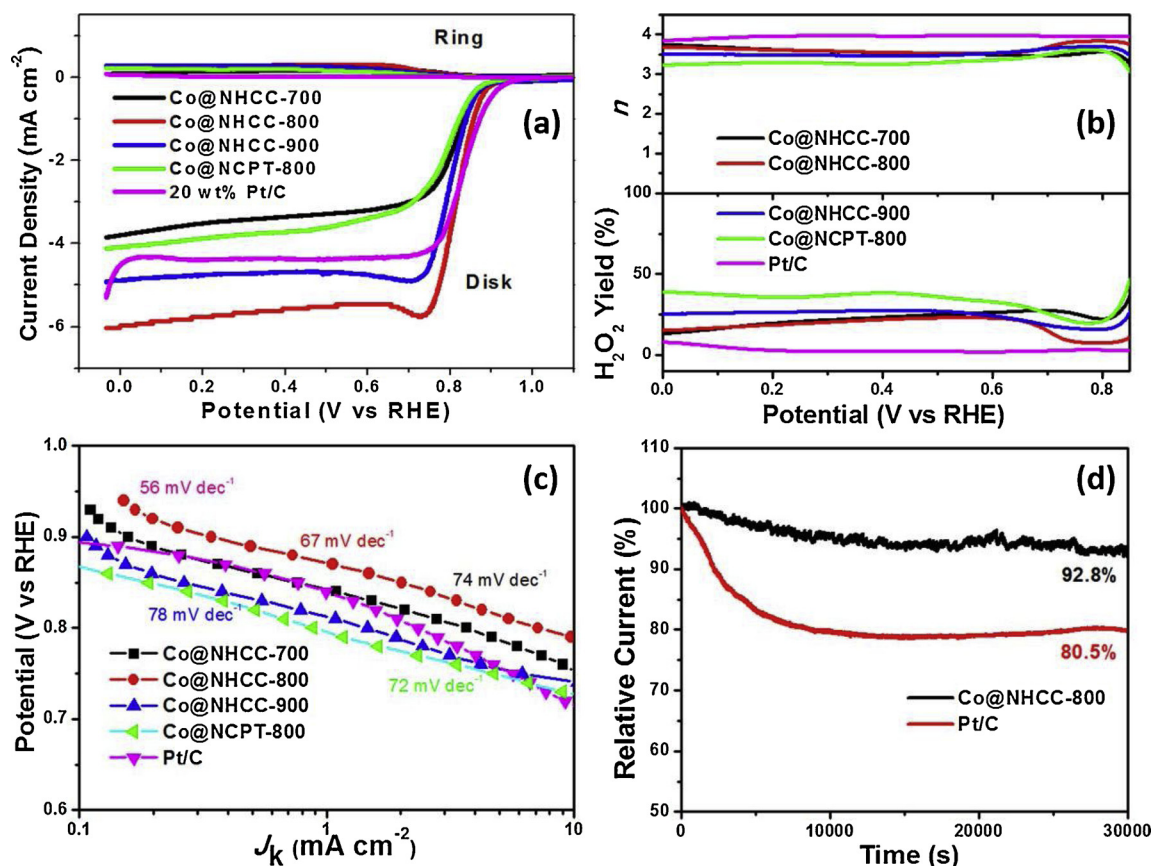

Fig. 3. (a) N₂ adsorption/desorption isotherms for different catalysts. (b) The pore size distribution curves of different catalysts.

Fig. 4. (a) RRDE voltammograms for Co@NHCC-T, Co@NCPT-800 and commercial Pt/C catalyst determined in oxygen-saturated 0.1 M KOH aqueous solution at an electrode rotation rate of 1600 rpm with a potential sweep rate of 10 mV s^{-1}. (b) The corresponding plots of electron transfer number and hydrogen peroxide yield, and (c) Tafel plots of different catalysts. (d) The chronoamperometric curves determined at +0.500 V for 30,000 s.

rechargeable metal-air batteries [69–71]. As depicted in Fig. 5a, one can find a sudden increase in the voltammetric current for all the investigated samples due to appearance of OER when the electrode potential is positively swept from +1.050 V to +1.700 V. Specifically, to achieve a current density of 10 mA cm^{-2}, an electrode bias of only +1.512 V is required for Co@NHCC-800 sample, which is the lowest as compared with the +1.601 V for Co@NHCC-700 and +1.576 V for Co@NHCC-900. Moreover, this value is lower than that of Co@NCPT-800 (+1.594 V) and even the benchmark RuO$_2$ catalyst (+1.550 V). These results confirm that Co@NHCC-800 shows the highest catalytic activity towards OER among the series and also demonstrate the importance role of dense assembly of silica nanoparticles on ZIF-67 polyhedron crystal surface in attaining high OER catalytic activity.

In the corresponding Tafel plots shown in Fig. 5b, the Co@NHCC-800 sample showed a slope of 84.2 mV/dec, a value that is close to that of RuO$_2$ catalyst (78.4 mV/dec) but slightly lower than the 86.0 mV/dec for Co@NHCC-700, 92.5 mV/dec for Co@NHCC-900, and 87.6 mV/dec for Co@NCPT-800, indicative of an improved reaction kinetics and bubble-releasing ability for Co@NHCC-800 in OER as compared with the other series catalysts. Additionally, from the series electrochemical impedance spectra depicted in Fig. 5c, one can find that the Co@NHCC-800 shows the smallest semicircle, as compared with all the investigated samples, including commercial RuO$_2$, which suggests that the OER proceeded on Co@NHCC-800 requires the lowest activation energy.

The working stability of Co@NHCC-800 in OER electrocatalysis was evaluated by chronoamperometric test at +1.600 V in 1 M KOH aqueous solution. As shown in Fig. 5d, although the current of electrode modified with Co@NHCC-800 drastically decreases to about 83% of its initial value at the very beginning of measurement, it shows nearly

negligible degradation rate during the subsequent measurements, leading to a retention of about 80% of its initial current value after continuously operating for 12 h. In sharp contrast, the reference electrode that is modified with RuO$_2$ shows a gradually decay in current, and can only maintain about 50.0% of its initial current value after working for 12 h. This observation signifies that Co@NHCC-800 has higher operation stability than the commercial RuO$_2$ catalyst.

The effects of additional utilization of C3N4 is also studied. Normally, a relatively high content of nitrogen in the final carbonized products is necessary to ensure a high oxygen electrocatalytic activity, including ORR and OER, because the nitrogen atoms in the graphitic carbon skeletons are considered to serve as active sites for both ORR and OER in N-doped carbons [42,43,72], as mentioned above. The nitrogen in the ligand, i.e. 2-methylimidazole, is highly volatile, which usually leads to low nitrogen content in the resulting carbonized products if there is no additional nitrogen source during pyrolysis. In present work, C$_3$N$_4$ is rich in nitrogen, and relatively stable at high temperature, which starts to decompose at about 600 °C, and completely decompose at 700 °C [73,74]. Hence, nitrogen decomposed from C$_3$N$_4$ at high temperature can dope into the carbonized ZIF-67 polyhedrons, leading to a relatively high content of nitrogen in the final products for efficient electrocatalysis. Without the presence of C$_3$N$_4$ during synthesis process, the resulting carbon-based electrocatalysts show lower catalytic activities for both OER and ORR, as evidenced by the results depicted in Fig. 6a–b.

Although the catalytic activities of Co@NHCC-800 sample are among the best nonprecious bifunctional electrocatalysts recently reported in literature (Table S1), determination of its active sites still needs further investigations. As depicted in Fig. 6, after leaching with HCl solution, the ORR limiting current of Co@NHCC-800 sample is
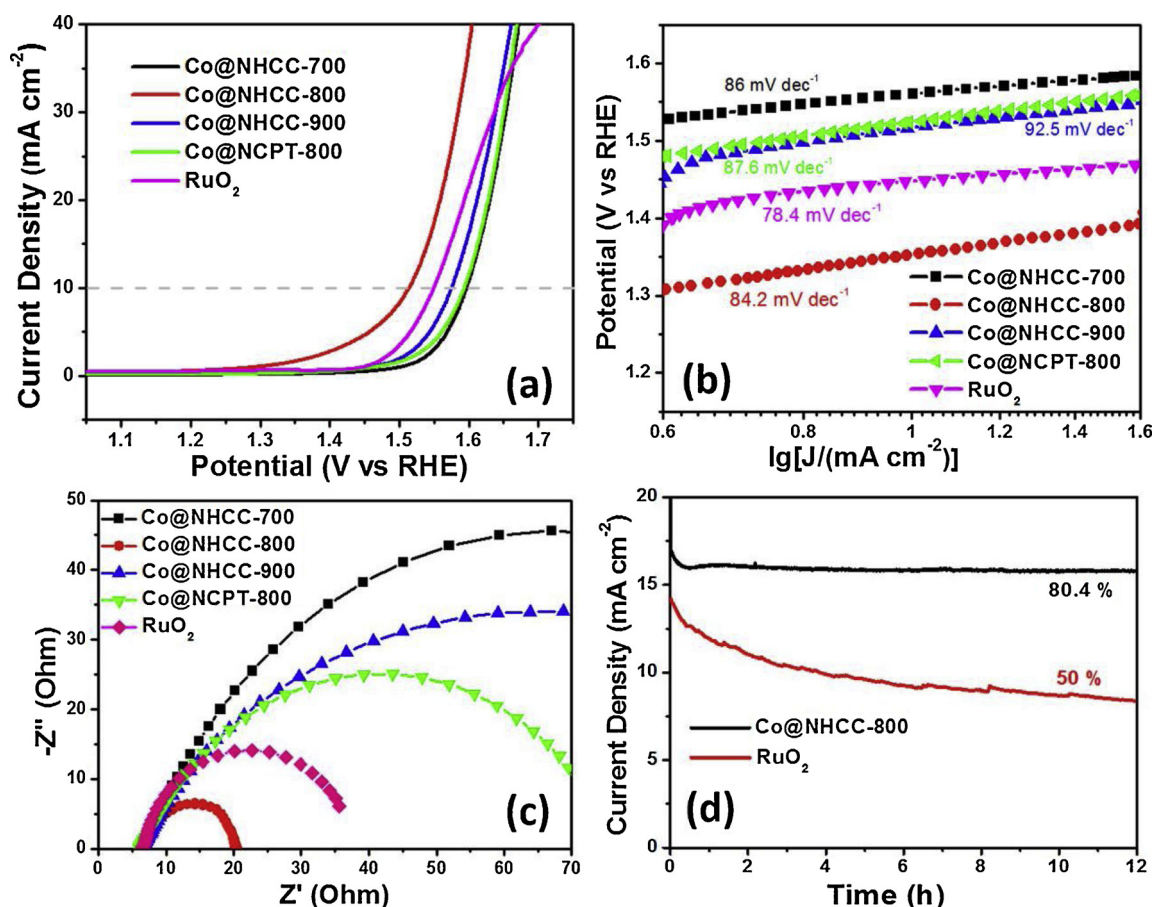
Fig. 5. (a) LSV curves for showing the OER catalytic activity of different samples in 1.0 M KOH aqueous solution at an electrode potential scanning rate of 10 mV s^{-1}. (b) The corresponding Tafel plots for different catalysts. (c) The electrochemical impedance spectra for the different catalysts loaded on a GCE electrode. Measurements were conducted at +1.550 V vs. RHE in a 1.0 M KOH aqueous solution with an AC amplitude of 5 mV as well as a frequency ranging from 10.00 kHz to 0.01 Hz. (d) Comparing the long-term OER operation stability of Co@NHCC-800 with commercial RuO$_2$ catalyst at +1.600 V.

markedly decreased, while the OER current at 10 mA/cm^2 is only slightly shifted towards a more positive value, indicating that metallic Co nanoparticles only contribute to partial of the ORR activities in Co@NHCC-800 sample but their contributions to OER is trivial. On basis of the above observations, we conclude that the single atom species such as Co-Nx-C [35,37,75] and N-C (probably graphitic N or pyridinic N) on the graphitized carbon skeletons [43,72,76] should mainly contribute to the efficient oxygen electrocatalysis.

Considering the excellent activity and operation durability of Co@

NHCC-800 towards oxygen reversible electrocatalysis, it shows high potential application in Zn-air batteries. Fig. 7a depicts the schematic of a representative Zn-air battery in present study, where Zn plate is utilized as the anode and catalysts deposited on hydrophobic carbon cloth are employed as air cathodes. To ensure the high reversibility of electrochemical reactions, an aqueous solution containing 6.0 M KOH and 0.2 M zinc acetate was used as electrolyte. For the primary Zn-air battery employing an Co@NHCC-800 based air cathode, it shows a stable open-circuit voltage of 1.490 V (Fig. 7b), which is markedly higher and
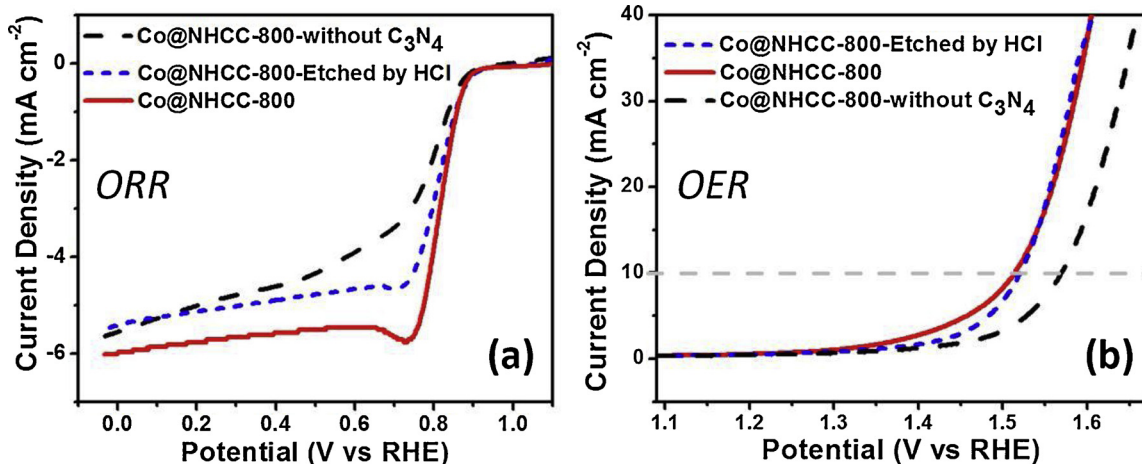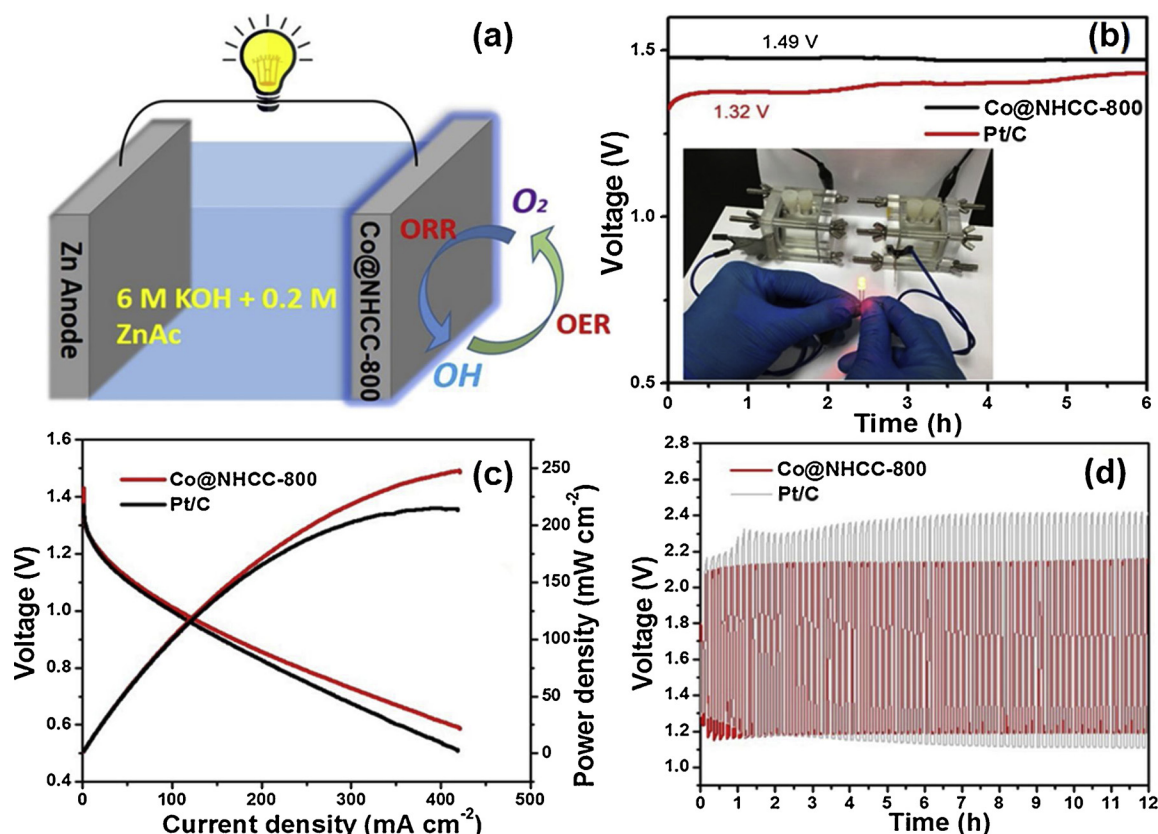

Fig. 6. (a) ORR and (b) OER LSV curves for Co@NHCC-800 samples prepared with or without the presence of C$_3$N$_4$, and etched by HCl.

Fig. 7. (a) A sketch for showing the device structure of a rechargeable Zn-air battery. (b) Plots showing the evolution of open-circuit voltage of rechargeable Zn-air batteries employing Co@NHCC-800 or Pt/C as air breathable cathodes. Inset to this panel is a photograph showing a LED lit by two rechargeable Zn-air batteries connected in series. (c) The discharge polarization curves of the primary Zn-air batteries and the corresponding power density. (d) Continuously charging and discharging Zn-air batteries with different air cathodes for 12 h at 10 mA cm^{-2}. Both the discharge and charge intervals were set for 5 min.

more stable than that utilizing commercial Pt/C (20 wt.%) catalyst as air cathode (1.320 V). With two Zn-air batteries connecting in series, a light-emitting diode (LED, with a nominal working voltage of ca. 3.0 V) can be lit (inset to panel b). In the discharge curves depicted in Fig. 7c, the battery with a Co@NHCC-800 based air cathode displays a higher output voltage than that comprising a commercial Pt/C (20 wt.%) based air cathode at various current density. Moreover, the Co@NHCC-800 exhibits a maximum power density of 248 mW cm^{-2}, also much higher than that of Pt/C (20 wt.%) catalyst (214 mW cm^{-2}). Fig. 7d depicts the voltage evolution of Co@NHCC-800 and Pt/C during charge-discharge process. At the beginning, the charge-discharge voltage gap is about 0.830 V for Co@NHCC-800, that is lower than the 0.860 V for Pt/C. After a continuous galvanostatic charge–discharge measurement for 12 h, the charge–discharge voltage gap is gradually increased to about 0.930 V, while a significantly larger value of 1.300 V is observed for Pt/C, indicative of a superior operation stability for Co@NHCC-800 as breathable air-cathode in rechargeable Zn-air batteries.

After charge-discharge cycling for 12 h in the above rechargeable Zn-air battery, the elemental contents of N, Co are decreased (Fig. 8a, Table 1) but the polyhedron-like morphology of Co@NHCC-800 bifunctional electrocatalyst is largely retained (Fig. 8b), indicating the high stability of this Co@NHCC-800 sample.

4. Conclusion

In conclusion, Co@NHCC samples were successfully prepared via directly pyrolyzing Co-MOFs polyhedron nanocrystals with the presence of dense silica nanoparticles and additional high-temperature decomposable nitrogen source g-C$_3$N$_4$. The dense silica nanoparticles on ZIF-67 polyhedron crystals can act as a hard encapsulation layer,

which not only drastically impede the growth of CNTs, but also effectively mitigate the collapse and fusion of these Co-MOFs nanocrystals, and hence helps preserve the polyhedron-like morphology. Concurrently, the release of volatile species from the inner parts of Co-MOFs nanocrystals during carbonization process facilitates the formation of hollow carbon cages, and finally contributes to a remarkably higher surface area of 910.71 m^2 g^{-1} in the resulting Co@NHCC-800 samples, as compared with the 367.94 m^2 g^{-1} of the control sample Co@NCPT-800 that is prepared without the presence of silica nanoparticles. The morphological merits, together with the high content of atomically dispersed nitrogen and Co-Nx-C species, lead to apparently bifunctional electrocatalysts towards ORR and OER, and Co@NHCC-800 is the best among the series, which shows a half-wave potential of +0.837 V for ORR in O$_2$-saturated 0.1 M KOH aqueous solution, a required potential of only +1.512 V that is lower than the benchmark RuO$_2$ to achieve a current density of 10 mA cm^{-2} in 1.0 M KOH aqueous solution. When Co@NHCC-800 is utilized as an air breathable electrode for Zn-air battery, it shows a much higher open-circuit voltage of 1.490 V and a higher discharge power density of 248 mW cm^{-2} than Pt/C catalyst. After a continuous galvanostatic charge–discharge measurement for 12 h, the polyhedron-like morphology of Co@NHCC-800 catalyst was largely retained, and charge–discharge voltage gap was slightly increased from +0.830 V to about +0.930 V, while a significantly increase from +0.860 V to +1.300 V was observed for Pt/C catalyst, signifying the high operation stability of Co@NHCC-800 as breathable air-cathode in rechargeable Zn-air batteries. These results not only highlight the high potential widespread application of Co@NHCC-800 in rechargeable Zn-air batteries, but also provide an effective approach to tailoring the morphology of carbon nanomaterials for more efficient electrocatalysis.
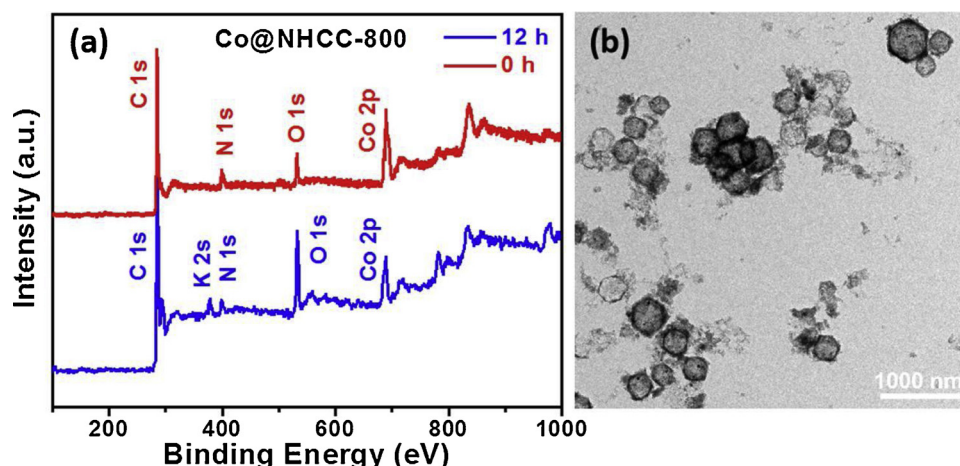
Fig. 8. (a) The XPS survey scans for Co@NHCC-800 sample before and after operation in a rechargeable Zn-air battery for 12 h. (b) The TEM image for showing the morphology of Co@NHCC-800 sample after operation in a rechargeable Zn-air battery for 12 h.

Appendix A. Supplementary data

Supplementary material related to this article can be found, in the online version, at doi:https://doi.org/10.1016/j.apcatb.2019.04.064.

References

[1] Z.L. Deng, Q.F. Yi, G. Li, Y. Chen, X.K. Yang, H.D. Nie, Electrochim. Acta 279 (2018) 1–9.
[2] Y. Li, H. Dai, Chem. Soc. Rev. 43 (2014) 5257–5275.
[3] M. Shao, Q. Chang, J.P. Dodelet, R. Chenitz, Chem. Rev. 116 (2016) 3594–3657.
[4] J. Yan, Q. Wang, T. Wei, Z. Fan, Adv. Energy Mater. 4 (2014) 1300816.
[5] Z.H. Li, M.F. Shao, L. Zhou, Q.H. Yang, C. Zhang, M. Wei, D.G. Evans, X. Duan, Nano Energy 25 (2016) 100–109.
[6] Y. Lv, L. Yang, D. Cao, ACS Appl. Mater. Interfaces 9 (2017) 32859–32867.
[7] K.P. Singh, E.J. Bae, J.S. Yu, J. Am. Chem. Soc. 137 (2015) 3165–3168.
[8] M. Dhelipan, A. Arunchander, A.K. Sahu, D. Kalpana, J. Saudi Chem. Soc. 21 (2017) 487–494.
[9] J.T. Zhang, L.T. Qu, G.Q. Shi, J.Y. Liu, J.F. Chen, L.M. Dai, Angew. Chem. Int. Ed. 55 (2016) 2230–2234.
[10] A. Gabe, J. Garcia-Aguilar, A. Berenguer-Murcia, E. Morallon, D. Cazorla-Amoros, Appl. Catal. B-Environ. 217 (2017) 303–312.
[11] X. Wang, L. Figueroa-Cosme, X. Yang, M. Luo, J.Y. Liu, Z.X. Xie, Y.N. Xia, Nano Lett. 16 (2016) 1467–1471.
[12] V. Beermann, M. Gocyla, E. Willinger, S. Rudi, M. Heggen, R.E. Dunin-Borkowski, M.G. Willinger, P. Strasser, Nano Lett. 16 (2016) 1719–1725.
[13] L.H. Zhuang, L. Ge, Y.S. Yang, M.R. Li, Y. Jia, X.D. Yao, Z.H. Zhu, Adv. Mater. 29 (2017) 1606793.
[14] Y. Ping, R.J. Nielsen, W.A. Goddard, J. Am. Chem. Soc. 139 (2017) 149–155.
[15] T. Audichon, T.W. Napporn, C. Canaff, C. Morais, C. Comminges, K.B. Kokoh, J. Phys. Chem. C 120 (2016) 2562–2573.
[16] X.X. Zou, Y. Zhang, Chem. Soc. Rev. 44 (2015) 5148–5180.
[17] W.M. Wu, X.Y. Wu, L. Zhang, J.H. Xiong, L. Wu, C.Z. Lu, Int. J. Hydrogen Energy 41 (2016) 139–144.
[18] J. Zhao, Y.C. Zou, X.X. Zou, T.Y. Bai, Y.P. Liu, R.Q. Gao, D.J. Wang, G.D. Li, Nanoscale 6 (2014) 7255–7262.
[19] M. Jahan, Z.L. Liu, K.P. Loh, Adv. Funct. Mater. 23 (2013) 5363–5372.
[20] C.G. Hu, L.M. Dai, Adv. Mater. 29 (2017) 9.
[21] J. Liu, L.G. Li, W.H. Niu, N. Wang, D.K. Zhao, S.B. Zeng, S.W. Chen, ChemElectroChem 3 (2016) 1116–1123.
[22] Y. Jia, L.Z. Zhang, G.P. Gao, H. Chen, B. Wang, J.Z. Zhou, M.T. Soo, M. Hong, X.C. Yan, G.R. Qian, J. Zou, A.J. Du, X.D. Yao, Adv. Mater. 29 (2017) 8.
[23] Y. Zheng, Y. Jiao, S.Z. Qiao, Adv. Mater. 27 (2015) 5372–5378.
[24] J.T. Zhang, L.M. Dai, Angew. Chem. Int. Ed. 55 (2016) 13296–13300.

[25] X. Zhang, R.R. Liu, Y.P. Zang, G.Q. Liu, G.Z. Wang, X. Zhang, H.M. Zhang, H.J. Zhao, Chem. Commun. 52 (2016) 5946–5949.
[26] J.T. Zhang, Z.H. Zhao, Z.H. Xia, L.M. Dai, Nat. Nanotechnol. 10 (2015) 444–452.
[27] R. Jiang, J. Fan, L. Hu, Y. Dou, X. Mao, D. Wang, Electrochim. Acta 261 (2018) 578–587.
[28] Y.C. Wang, Y.J. Lai, L. Song, Z.Y. Zhou, J.G. Liu, Q. Wang, X.D. Yang, C. Chen, W. Shi, Y.P. Zheng, M. Rauf, S.G. Sun, Angew. Chem. Int. Ed. 54 (2015) 9907–9910.
[29] D.W. Kong, W.J. Yuan, C. Li, J.M. Song, A.J. Xie, Y.H. Shen, Appl. Surf. Sci. 393 (2017) 144–150.
[30] C.Z. Zhu, H. Li, S.F. Fu, D. Du, Y.H. Lin, Chem. Soc. Rev. 45 (2016) 517–531.
[31] W. Xia, A. Mahmood, R.Q. Zou, Q. Xu, Energy Environ. Sci. 8 (2015) 1837–1866.
[32] J. Liu, Y. Liu, N.Y. Liu, Y.Z. Han, X. Zhang, H. Huang, Y. Lifshitz, S.T. Lee, J. Zhong, Z.H. Kang, Science 347 (2015) 970–974.
[33] H.C. Zhou, J.R. Long, O.M. Yaghi, Chem. Rev. 112 (2012) 673–674.
[34] W. Niu, L. Li, X. Liu, N. Wang, J. Liu, W. Zhou, Z. Tang, S. Chen, J. Am. Chem. Soc. 137 (2015) 5555–5562.
[35] H.L. Fei, J.C. Dong, Y.X. Feng, C.S. Allen, C.Z. Wan, B. Volosskiy, M.F. Li, Z.P. Zhao, Y.L. Wang, H.T. Sun, P.F. An, W.X. Chen, Z.Y. Guo, C. Lee, D.L. Chen, I. Shakir, M.J. Liu, T.D. Hu, Y.D. Li, A.I. Kirkland, X.F. Duan, Y. Huang, Nat. Catal. 1 (2018) 63–72.
[36] P. Chen, T. Zhou, L. Xing, K. Xu, Y. Tong, H. Xie, L. Zhang, W. Yan, W. Chu, C. Wu, Y. Xie, Angew. Chem. Int. Ed. 56 (2017) 610–614.
[37] Y. He, S. Hwang, D.A. Cullen, M.A. Uddin, L. Langhorst, B. Li, S. Karakalos, A.J. Kropf, E.C. Wegener, J. Sokolowski, M. Chen, D. Myers, D. Su, K.L. More, G. Wang, S. Litster, G. Wu, Energy Environ. Sci. 12 (2019) 250–260.
[38] Y. Luo, J. Zhang, M. Kiani, Y. Chen, J. Chen, G. Wang, S.H. Chan, R. Wang, Ind. Eng. Chem. Res. 57 (2018) 12087–12095.
[39] H. Zhong, Y. Luo, S. He, P. Tang, D. Li, N. Alonso-Vante, Y. Feng, ACS Appl. Mater. Interfaces 9 (2017) 2541–2549.
[40] J. Li, N. Zhou, J. Song, S. Fu, J. Yan, Y. Tang, H. Wang, ACS Sustainable Chem. Eng. 6 (2018) 413–421.
[41] H.B. Yang, J. Miao, S.-F. Hung, J. Chen, H.B. Tao, X. Wang, L. Zhang, R. Chen, J. Gao, H.M. Chen, L. Dai, B. Liu, Sci. Adv. 2 (2016) e1501122.
[42] K. Mamtani, D. Jain, D. Dogu, V. Gustin, S. Gunduz, A.C. Co, U.S. Ozkan, Appl. Catal. B-Environ. 220 (2018) 88–97.
[43] H. Jiang, J.X. Gu, X.S. Zheng, M. Liu, X.Q. Qiu, L.B. Wang, W.Z. Li, Z.F. Chen, X.B. Ji, J. Li, Energy Environ. Sci. 12 (2019) 322–333.
[44] L. Shang, H. Yu, X. Huang, T. Bian, R. Shi, Y. Zhao, G.I. Waterhouse, L.Z. Wu, C.H. Tung, T. Zhang, Adv. Mater. 28 (2016) 1668–1674.
[45] Z. Li, W. Wang, H. Cao, Q. Zhang, X. Zhou, D. Wang, Y. Wang, S. Zhang, G. Zhang, C. Liu, Y. Zhang, R. Liu, J. Jiang, Adv. Mater. Technol. 2 (2017) 1700224.
[46] S.C. Cai, Z.H. Meng, H.L. Tang, Y. Wang, P. Tsiakaras, Appl. Catal. B-Environ. 217 (2017) 477–484.
[47] Y.L. Zhou, J. Miao, Y.H. Shen, A.J. Xie, Appl. Surf. Sci. 453 (2018) 83–92.
[48] B.X. Zhang, H. Gao, X.L. Li, New J. Chem. 38 (2014) 4615–4621.
[49] N. Wang, B. Lu, L. Li, W. Niu, Z. Tang, X. Kang, S. Chen, ACS Catal. 8 (2018) 6827–6836.
[50] N. Wang, L. Li, D. Zhao, X. Kang, Z. Tang, S. Chen, Small 13 (2017) 1701025.
[51] S. Dou, L. Tao, J. Huo, S. Wang, L. Dai, Energy Environ. Sci. 9 (2016) 1320–1326.
[52] J.W. Su, Y. Yang, G.L. Xia, J.T. Chen, P. Jiang, Q.W. Chen, Nat. Commun. 8 (2017) 10.
[53] L.L. Feng, M.H. Fan, Y.Y. Wu, Y.P. Liu, G.D. Li, H. Chen, W. Chen, D.J. Wang, X.X. Zou, J. Mater. Chem. A 4 (2016) 6860–6867.
[54] J. Wei, Y.X. Hu, Y. Liang, B.A. Kong, J. Zhang, J.C. Song, Q.L. Bao, G.P. Simon, S.P. Jiang, H.T. Wang, Adv. Funct. Mater. 25 (2015) 5768–5777.
[55] L.F. Zhai, S.Y. Kong, H.Y. Zhang, W.J. Tian, M. Sun, H.Q. Sun, S.B. Wang, Chem. Eng. Sci. 194 (2019) 45–53.
[56] P. Ganesan, M. Prabu, J. Sanetuntikul, S. Shanmugam, ACS Catal. 5 (2015) 3625–3637.

[57] W. Ding, L. Li, K. Xiong, Y. Wang, W. Li, Y. Nie, S.G. Chen, X.Q. Qi, Z.D. Wei, J. Am. Chem. Soc. 137 (2015) 5414–5420.

[58] S.T. Hunt, M. Milina, A.C. Alba-Rubio, C.H. Hendon, J.A. Dumesic, Y. Roman-Leshkov, Science 352 (2016) 974–978.

[59] Q. Liu, J.Q. Tian, W. Cui, P. Jiang, N.Y. Cheng, A.M. Asiri, X.P. Sun, Angew. Chem. Int. Ed. 53 (2014) 6710–6714.

[60] Y.Z. Chen, C.M. Wang, Z.Y. Wu, Y.J. Xiong, Q. Xu, S.H. Yu, H.L. Jiang, Adv Mater. 27 (2015) 5010–5016.

[61] Z. Cheng, J. Gao, Q. Fu, C. Li, X. Wang, Y. Xiao, Y. Zhao, Z. Zhang, L. Qu, ACS Appl. Mater. Interfaces 9 (2017) 24608–24615.

[62] Z.Q. Liu, H. Cheng, N. Li, T.Y. Ma, Y.Z. Su, Adv. Mater. 28 (2016) 3777–3784.

[63] X. Zheng, X. Cao, X. Li, J. Tian, C. Jin, R. Yang, Nanoscale 9 (2017) 1059–1067.

[64] J. Wu, J. Liu, L. Li, X. Wang, J. Mater. Sci. 52 (2017) 9794–9805.

[65] J. Sanetuntikul, C. Chuaicham, Y.W. Choi, S. Shanmugam, J. Mater. Chem. A 3 (2015) 15473–15481.

[66] J. Yu, C. Wang, W. Yuan, Y. Shen, A. Xie, Chemistry 25 (2019) 2877–2883.

[67] W. Niu, L. Li, J. Liu, N. Wang, W. Li, Z. Tang, W. Zhou, S. Chen, Small 12 (2016) 1900–1908.

[68] Z. Zong, K. Xu, D. Li, Z. Tang, W. He, Z. Liu, X. Wang, Y. Tian, J. Catal. 361 (2018) 168–176.

[69] J. Wang, H.H. Wu, D.F. Gao, S. Miao, G.X. Wang, X.H. Bao, Nano Energy 13 (2015) 387–396.

[70] N.T. Suen, S.F. Hung, Q. Quan, N. Zhang, Y.J. Xu, H.M. Chen, Chem. Soc. Rev. 46 (2017) 337–365.

[71] S.W. Li, S.J. Peng, L.S. Huang, X.Q. Cui, A.M. Al-Enizi, G.F. Zheng, ACS Appl. Mater. Interfaces 8 (2016) 20534–20539.

[72] H.B. Yang, J.W. Miao, S.F. Hung, J.Z. Chen, H.B. Tao, X.Z. Wang, L.P. Zhang, R. Chen, J.J. Gao, H.M. Chen, L.M. Dai, B. Liu, Sci. Adv. 2 (2016) 11.

[73] H.Y. Li, S.Y. Gan, H.Y. Wang, D.X. Han, L. Niu, Adv. Mater. 27 (2015) 6906–6913.

[74] A. Kumar, P. Kumar, R. Borkar, A. Bansiwal, N. Labhsetwar, S.L. Jain, Carbon 123 (2017) 371–379.

[75] P.Z. Chen, T.P. Zhou, L.L. Xing, K. Xu, Y. Tong, H. Xie, L.D. Zhang, W.S. Yan, W.S. Chu, C.Z. Wu, Y. Xie, Angew. Chem. Int. Ed. 56 (2017) 610–614.

[76] K. Mamtani, D. Jain, D. Dogu, V. Gustin, S. Gunduz, A.C. Co, U.S. Ozkan, Appl. Catal. B-Environ. 220 (2018) 88–97.